Desalination and Water Treatment
www.deswater.com

doi: 10.5004/dwt.2022.28863

273 (2022) 212–220
October

Combustion synthesis and analysis of visible-light-driven Ho-doped ZnO photocatalytic nanoparticles

Anukorn Phuruangrat[a,*], Suwanan Thamsukho[a], Titipun Thongtem[b,c], Somchai Thongtem[b,d,*]

[a]*Division of Physical Science, Faculty of Science, Prince of Songkla University, Hat Yai, Songkhla 90112, Thailand, Tel. +66 (0)74 288374; Fax: +66 (0)74 288395; emails: phuruangrat@hotmail.com (A. Phuruangrat), 5910210341@psu.ac.th (S. Thamsukhoa)*
[b]*Materials Science Research Center, Faculty of Science, Chiang Mai University, Chiang Mai 50200, Thailand, Tel. +66 (0)53 943367; Fax: +66 (0)53 943445; emails: schthongtem@yahoo.com (S. Thongtem), ttpthogntem@yahoo.com (T. Thongtem)*
[c]*Department of Chemistry, Faculty of Science, Chiang Mai University, Chiang Mai 50200, Thailand*
[d]*Department of Physics and Materials Science, Faculty of Science, Chiang Mai University, Chiang Mai 50200, Thailand*

Received 2 February 2022; Accepted 20 August 2022

ABSTRACT

ZnO nanoparticles with different Ho dopant were prepared by tartaric acid solution combustion method and followed by calcination at 600°C for 2 h. The XRD patterns of ZnO and Ho-doped ZnO samples were indexed to the pure phase of hexagonal wurtzite ZnO structure. TEM images of ZnO and Ho-doped ZnO showed that the samples were nanoparticles with different sizes. The particle size of sample was decreased with increasing in the weight content of Ho dopant. The XPS results certified that the Ho^{3+} ions contained in ZnO lattice. The photocatalytic activity of the as-synthesized ZnO nanoparticles with different Ho contents was evaluated through the degradation of methylene blue (MB) as a dye pollutant under visible light irradiation. The photodegradation of MB in aqueous medium under visible light irradiation showed that the 3% Ho-doped ZnO nanoparticles have the highest photocatalytic activity in degrading of MB molecules because Ho^{3+} ions played the role in trapping electrons, inhibiting the recombination charge carrier pairs and enhancing the photocatalytic performance of ZnO under visible light irradiation.

Keywords: Ho-doped ZnO; Photocatalytic property; Combustion synthesis

1. Introduction

In the recent years, decomposition of environmental pollutant and wastewater treatment using metal oxide semiconductors have attracted much attention because they are low cost, nontoxicity, environmentally friendly and long-term stability, including they have high catalytic activity [1–6]. Under light irradiation, electron–hole pairs in conduction band and valence band of semiconductor were separated and reacted with water and oxygen to produce hydroxyl radical ($^{\bullet}OH$) and superoxide anion radical ($^{\bullet}O_2^-$) [7–10]. These radicals can play the role in degrading organic compound such as pigments and dye molecules [7–10]. Among the various photocatalysts, ZnO as n-type semiconductor with band gap energy of 3.37 eV at room temperature shows very high photocatalytic efficiency in degrading of dyes such as methylene blue (MB) [7,8,11,12], methyl orange (MO) [10,13], rhodamine B (RhB) [14,15] and malachite green (MG) [16,17]. Nevertheless, photocatalytic efficiency of ZnO was limited because photo-excited electrons and photo-induced holes were rapidly recombined and ZnO was active in only UV light [1,2,12]. To solve the

* Corresponding authors.

problem, rare earth metal such as Ce [17,18], Dy [19,20], Eu [21,22], Gd [23,24] and Sm [25] was adopted to increase the photocatalytic efficiency of ZnO in degrading of dye under visible light irradiation [1,12,17,19,21]. Another rare earth element such as holmium (Ho) containing incomplete 4f orbital shows a great potential in improving the photocatalytic performance of the ceramic semiconductor by creating a new energy level within band gap because the surface segregation of Ho^{3+} ion can lead to create oxygen vacancies and trap photogenerated electrons [26–28]. Thus, visible light absorption of the semiconductor was increased and the recombination of e–h pairs was inhibited which led to enhance the photocatalytic activity [1,17,19,26–28].

In this work, a series of Ho-doped ZnO nanoparticles were prepared by combustion method. The photocatalytic efficiency of a series of Ho-doped ZnO nanoparticles in degrading of methylene blue (MB) under visible light irradiation was investigated. In addition, a possible photocatalytic mechanism of Ho-doped ZnO nanoparticles under visible light irradiation was proposed and discussed.

2. Experimental details

To prepare 0%–5% Ho doped ZnO, each 0.01 mol $Zn(NO_3)_2{\cdot}6H_2O$ and 0–5% $Ho(NO_3)_3{\cdot}6H_2O$ by weight were dissolved in 50 mL C_2H_5OH solutions under continued stirring. Subsequently, 0.01 mol tartaric acid in 50 mL C_2H_5OH solution was added to these solutions to form gel precursors. Then, 1 M 20 mL NaOH solution in C_2H_5OH solution was also added to them with continued stirring for 30 min. The as-synthesized gel precursors were filtered, washed with distilled water and dried at 80°C for 12 h. Subsequently, the dried precursor was calcined in air at 600°C for 2 h.

The dried precursor was analyzed by thermogravimetric analysis (STA 8000 Simultaneous Thermal Analyzer, TGA, PerkinElmer) in nitrogen atmosphere with 10°C.min^{-1} heating rate at room temperature (T_R) – 800°C. The phase of products was characterized by X-ray diffraction (XRD) on a Philips X'Pert MPD X-ray diffractometer equipped with Cu K_α radiation ranging from 10° to 80° at a scanning rate of 0.005 deg/s. The morphology and phase were characterized by transmission electron microscopy (TEM) and selected area electron diffraction (SAED) taken on a JEOL, JEM 2010 TEM at an acceleration voltage of 200 kV. Fourier transform infrared spectroscopic (FTIR) spectra of samples were analyzed by a Bruker Tensor 27 FTIR spectrometer at 400–4,000 cm^{-1} with 4 cm^{-1} resolution. Raman spectra of samples were analyzed by a T64000 HORIBA Jobin Yvon Raman spectrometer using Ar green laser at 514.5 nm wavelength. The surface oxidation state of element was analyzed by Axis Ultra DLD|Kratos–Kratos Analytical X-ray photoelectron spectroscopy (XPS) using the monochromated Al K_α radiation (1486.6 eV) as a providing source and C1s electron peak at 285.0 eV as a reference. The optical property of samples was studied by a PerkinElmer Lambda 25 UV-visible spectrometer at room temperature. The Brunauer–Emmett–Teller (BET) surface area of the photocatalyst was determined by Micromeritics ASAP 2460 Surface Area and Porosity Analyzer. Photoluminescence (PL) was carried out on a PerkinElmer LS 50B Fluorescence spectrometer.

Photocatalytic activities of the as-synthesized samples were tested by measuring the degradation of methylene blue (MB) in an aqueous solution under a visible radiation. The 0.5 g photocatalyst was suspended in a 500 mL of 2.5×10^{-5} M MB aqueous solution which was magnetically stirred in the dark for 30 min to establish an adsorption-desorption equilibrium of MB on the surface of the photocatalyst. Then the visible light from a xenon lamp was turned on to initiate photocatalysis. The solution was analyzed by a Lambda 25 spectrometer using a 450 W xenon lamp with wavelength of 664 nm as maximum absorption. The decolorization efficiency was calculated using:

$$\text{Decolorization efficiency}(\%) = \frac{C_o - C}{C_o} \times 100 \quad (1)$$

where C_o is the initial concentration of MB and C is the concentration of MB after light irradiation. The degree of dye mineralization was monitored by analyzing the total organic carbon content (TOC) in the MB solution using a multi N/C 3100 Analytik Jena GmbH analyzer.

3. Results and discussion

TGA graph of metal-tartaric complex precursor was analyzed at T_R–800°C with a heating rate of 10°C.min^{-1} in nirogen atmosphere as the results shown in Fig. 1. TGA graph of metal-tartaric complex precursor shows two steps of weight loss at T_R–247°C of moisture containing in the gel and crystallized water, and at 247°C–560°C decomposition temperature of tartaric acid into carbon oxide and water and residual nitrate group [11,26,29,30]. Above 560°C, the weight loss of precursors remains unchanged, indicating the formation of ZnO. In this research, the total weight losses were 49% for ZnO-tartaric complex and 58% for 5% Ho-doped ZnO-tartaric complex. Thus, the dried precursor was calcined at 600°C.

Fig. 2a shows XRD patterns of pure ZnO and Ho-doped ZnO samples synthetized by combustion method. All the

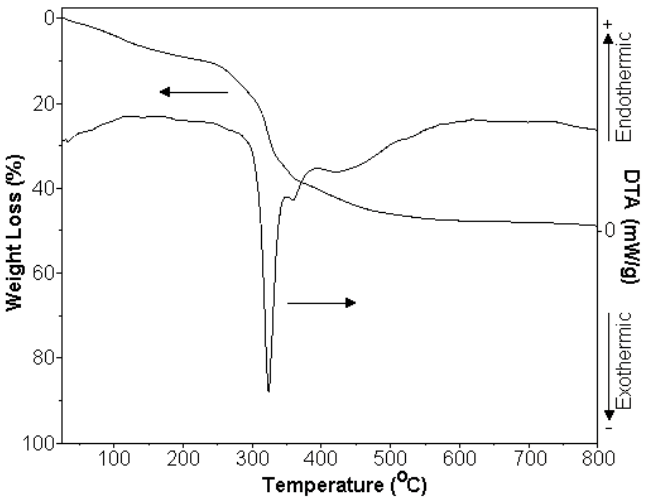

Fig. 1. TGA and DTA graphs of Zn-tartaric acid precursor at T_R–800°C in nitrogen atmosphere.

peaks of pure ZnO and Ho-doped ZnO samples can be indexed to the hexagonal wurtzite structure of ZnO as compared to the JCPDS No. 36-1451 [31]. There was no detection the diffraction peaks of impurities such as Ho_2O_3 in Ho-doped ZnO samples. The results indicated that Ho^{3+} ions were uniformly incorporated in the Zn^{2+} vacancies and interstitial sites of ZnO crystal. In this research, the diffraction peaks of Ho-doped ZnO samples were slight shifted to the lower angle comparing with that of pure ZnO sample (Fig. 2b) because the ionic radius of Ho^{3+} ion (1.072 Å [32–34]) is larger than the ionic radius of Zn^{2+} ion (0.74 Å [3,18–20,24,25]). The result certified the incorporation of Ho^{3+} ions in the ZnO host structure. The crystallite sizes of ZnO and Ho-doped ZnO samples were calculated by the Scherrer equation [1,3,10,15,19,22,24]. They were 36, 31, 28 and 27 nm for 0%, 1%, 3% and 5% Ho-doped ZnO samples, respectively. The mean size can be smaller or equal to the grain size and is controlled by the crystallite shape. The dimensionless shape factor K is close to unity but varies with the actual shape of the crystallite. The line broadening at half the maximum intensity is related to physical broadening and instrumental broadening [35,36].

Fig. 3a shows the Raman spectra of pure ZnO and Ho-doped ZnO samples synthetized by combustion method. According to the group theory, hexagonal ZnO belongs to the C^4_{6v} space group, the optical phonons at the Γ point of the Brillouin zone are $A_1 + 2B_1 + E_1 + 2E_2$ [8,14,19,24,25]. The typical modes of pure ZnO sample show the Raman peaks at 331, 380, 410, 438 and 581 cm^{-1} related to the E_2(high)–E_2(low), A_1(TO), E_1(TO), E_2(high) and E_1(LO), respectively [4,5,11,16,21,22]. The E_1(LO) is related to the defects such as V_O and Zn_i for Ho-doped ZnO. Thus, the photocatalytic performance in ZnO under visible light irradiation was enhanced [14,19,24,25,37].

Fig. 3b shows the FTIR spectra of pure ZnO, 3% Ho-doped ZnO and 5% Ho-doped ZnO samples synthetized by combustion method. They show the broad band at 3,200–3,400 cm^{-1} assigned to the stretching mode of O–H of adsorbed H_2O on the surface of pure ZnO and Ho-doped ZnO

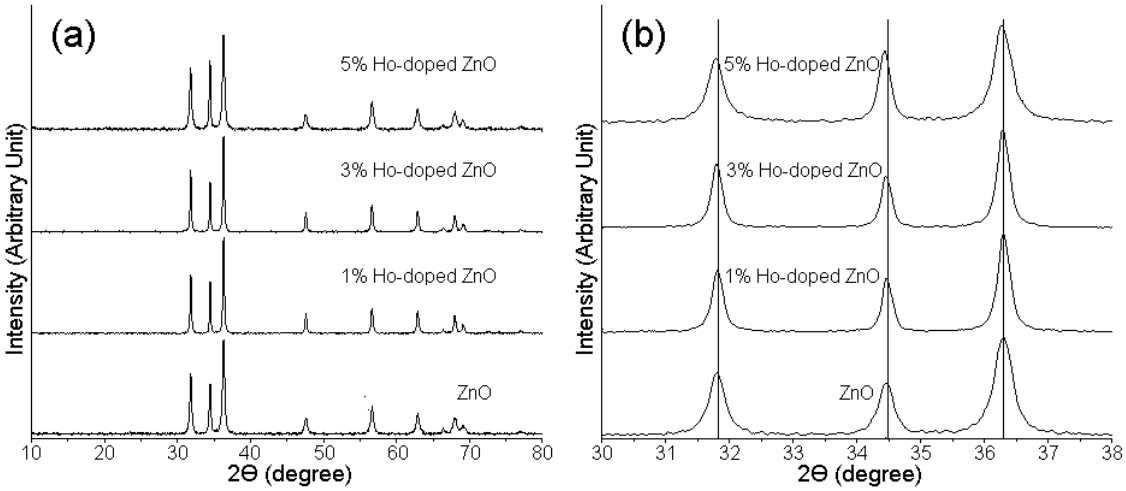

Fig. 2. XRD patterns of 0%–5% Ho-doped ZnO samples synthesized by a tartaric acid-assisted combustion method over the 2θ range of (a) 10°–80° and (b) 30°–38°.

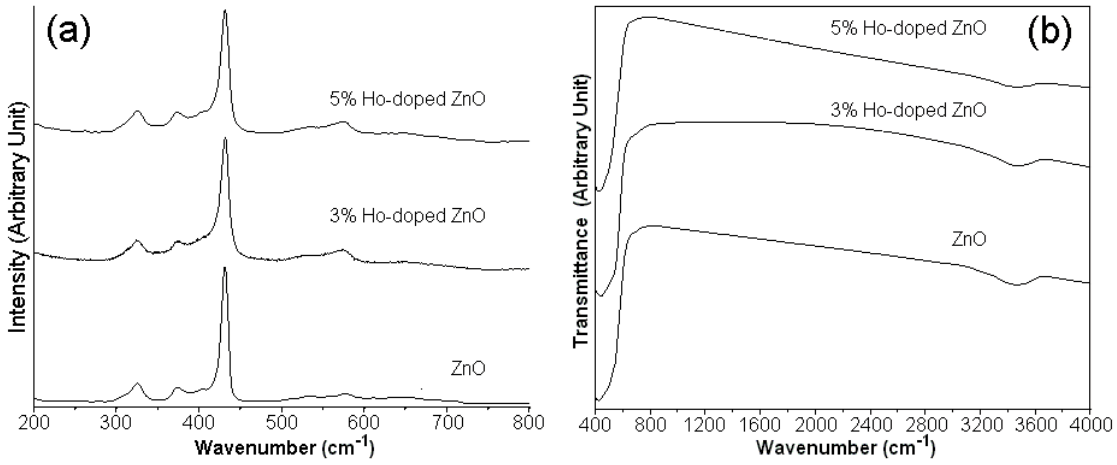

Fig. 3. (a) Raman and (b) FTIR spectra of pure ZnO, 3% and Ho-doped ZnO 5% Ho-doped ZnO samples.

samples [7,8,14,19,23]. There was detection of C–H stretching and bending vibrations of organic species, indicating that the tartaric acid was completely decomposed at 600°C for 2 h [2,9,14]. The FTIR spectra of pure ZnO and Ho-doped ZnO samples show the sharp peaks at 435 cm^{-1} related to the stretching vibration of Zn–O bond [7,8,14,19,23].

The chemical state and elemental composition of the 3% Ho-doped ZnO samples were characterized by X-ray photoelectron spectroscopy (XPS) and the results are shown in Fig. 4. The survey spectrum of as-prepared 3% Ho-doped ZnO sample (Fig. 4a) demonstrates the binding energy peaks of Ho 4d, Zn 2p and O 1s. The high resolution binding energy of Ho 4d orbital in 3% Ho-doped ZnO nanoparticles (Fig. 4b) was detected at 161.5 eV. It certifies that the oxidation state of Ho is trivalent which is consistent in the explanation of the previous reports [38,39]. The Zn $2p_{3/2}$ and Zn $2p_{1/2}$ core levels of 3% Ho-doped ZnO (Fig. 4c) were detected at 1,021.42 and 1,044.50 eV, respectively. This detection indicates that the oxidation state of Zn species is 2+ [17,19,23,40,41]. Fig. 4d shows the high resolution asymmetric binding energy of O 1s core level of as-prepared 3% Ho-doped ZnO nanoparticles. By Gaussian fitting, the asymmetric binding energies of O 1s core level of 3% Ho-doped ZnO sample were detected at 528.89, 530.44, 531.54 and 532.51 eV. They were related to the Zn–O bond, intrinsic O^{2-} ions in the wurtzite structure, oxygen-deficient in ZnO lattice and chemisorbed oxygen of H_2O on the top, respectively [17,19,23,40,41]. The XPS result confirms that Ho^{3+} ions exist in ZnO matrix. The weight percent of Ho in as-prepared 3% Ho-doped ZnO sample was 2.30%.

The morphology of ZnO and Ho-doped ZnO prepared by combustion method was investigated by TEM and the results are shown in Fig. 5. The TEM image of pure ZnO sample shows irregular particles with different sizes. The particle size range of pure ZnO sample was 50–200 nm. When Ho was doped in ZnO lattice, the particle size of ZnO was reduced. The particle size ranges were 50–100 nm, 10–25 nm and 10–20 nm for 1%, 3% and 5% Ho-doped ZnO samples, respectively. The average particle-sizes were 65.35 ± 24.65 nm, 23.22 ± 4.85 nm, 19.72 ± 4.84 nm and 15.78 ± 3.84 nm for 0%, 1%, 3% and 5% Ho-doped ZnO nanoparticles, respectively. The typical selected areas of electron diffraction (SAED) patterns of the ZnO and Ho-doped ZnO samples as inserted in Fig. 5 show the patterns of bright continued electron spots, indicating that all samples were highly crystalline. They can be indexed to the (100), (002), (101), (102), (110), (103), (112) and (201) planes of hexagonal wurtzite ZnO structure of the JCPDS No. 36-1451. In addition, the surface areas of photocatalysts determined by the BET analysis were 3.68, 28.92, 38.76 and 36.75 $m^2\ g^{-1}$ for 0%, 1%, 3% and 5% Ho-doped ZnO nanoparticles, respectively. The surface areas of samples were increased with decreasing in the particle sizes. It was the highest for 3%

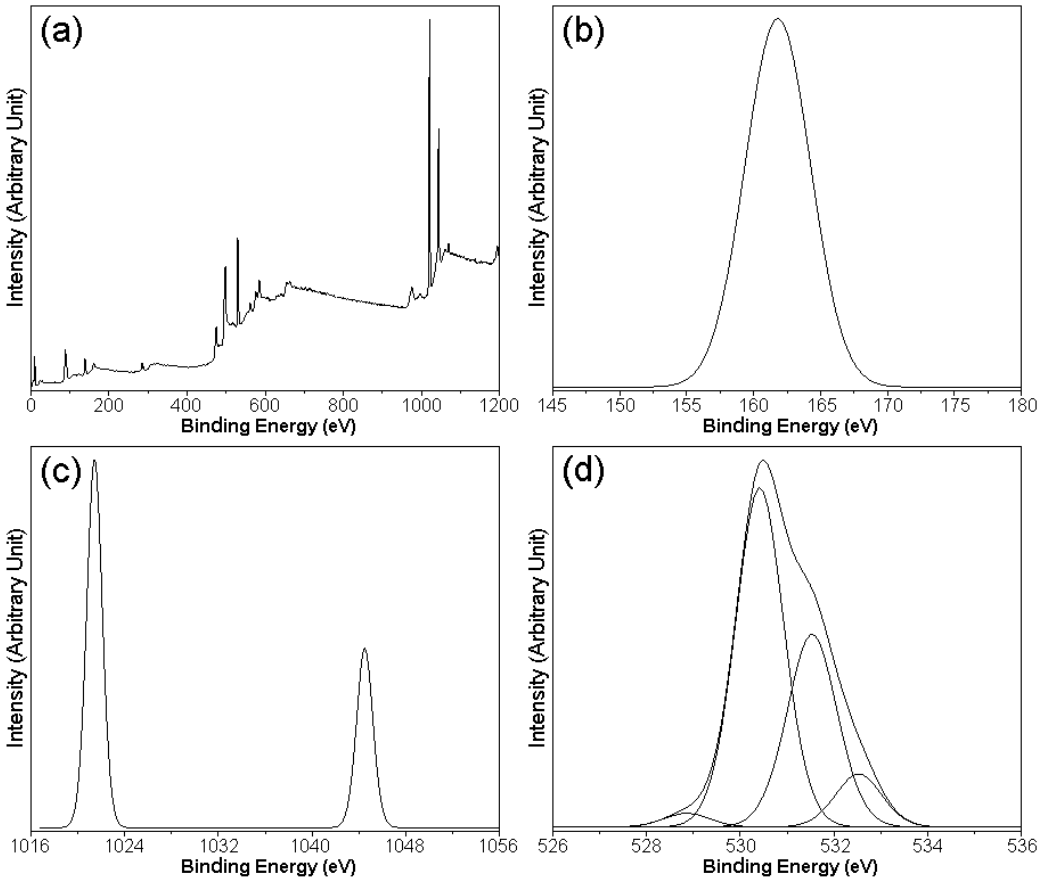

Fig. 4. (a) XPS survey spectrum and (b–d) high-resolution XPS spectra of Ho 4d, Zn 2p and O 1s of 3% Ho-doped ZnO, respectively.

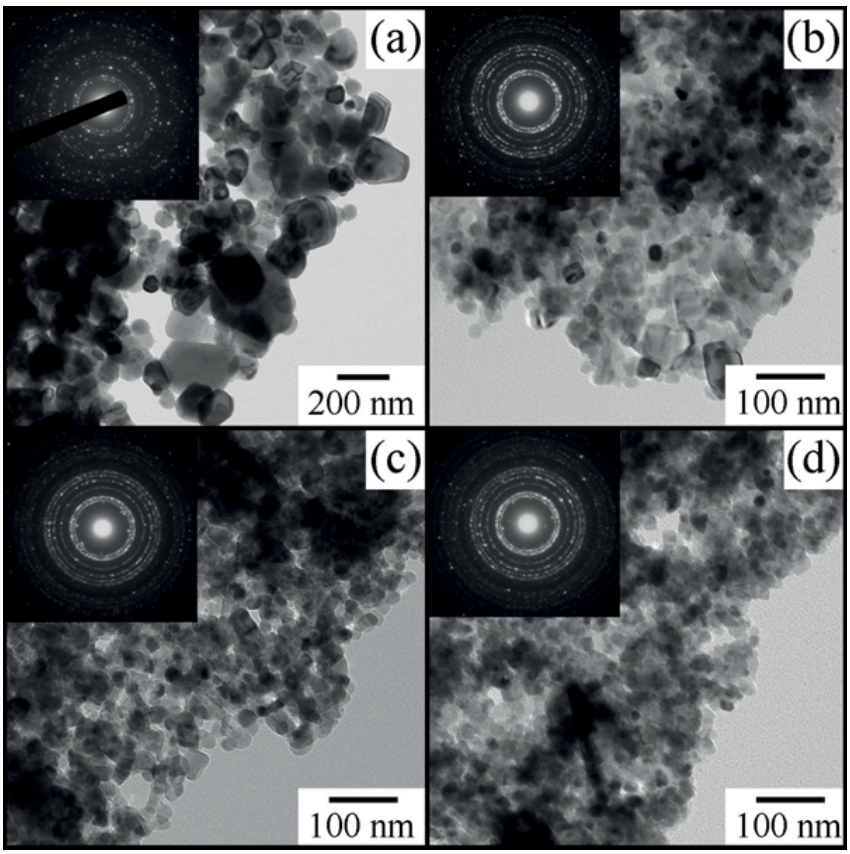

Fig. 5. TEM images and SAED patterns of the as-synthesized (a–d) 0%, 1%, 3% and 5% Ho-doped ZnO samples, respectively.

Ho-doped ZnO nanoparticles. Further increase of Ho content, the surface area of 5% Ho-doped ZnO nanoparticles became lessened because the high free surface energy of nanoparticles and the nanoparticles clustered together in groups [42].

Fig. 6 shows the UV-visible absorption of ZnO, 3% Ho-doped ZnO and 5% Ho-doped ZnO nanoparticles. The pure ZnO nanoparticles without Ho dopant show the strong absorption in UV region with a strong absorption at 362.24 nm wavelength [1,17,22]. The UV-visible absorbance of Ho-doped ZnO showed higher visible absorption and slightly red shifted toward the higher wavelength of 364.56 nm for 3% Ho-doped ZnO nanoparticles and 368.28 nm for 5% Ho-doped ZnO nanoparticles because of the presence of intermediate state between the valence and conduction bands of ZnO nanoparticles [1,2,9,17,22]. The band gaps (E_g) of ZnO and Ho-doped ZnO nanoparticles were determined using the $E_g = 1239.8031/\lambda$ [43–45]. They were 3.42, 3.40 and 3.37 eV for 0%, 3% and 5% Ho-doped ZnO nanoparticles, respectively. The band gap energy of Ho-doped ZnO nanoparticles was decreased because of the Burstain–Moss effect and Fermi level located in the conduction band of ZnO [2,9,17,22,23,26].

Fig. 7 shows the temporal change of the absorption spectra in degrading of MB dye over ZnO and 3% Ho-doped ZnO nanoparticles under visible light irradiation. Clearly, the maximum wavelength of MB at 664 nm over 3% Ho-doped ZnO nanoparticles was decreased faster than that over pure ZnO nanoparticles. The absorption of MB over 3% Ho-doped ZnO nanoparticles decreased to nearly zero within 150 min irradiation, implying that the MB molecules were completely degraded.

Fig. 8a shows the photocatalytic efficacies of MB degradation in the presence of ZnO and Ho-doped ZnO nanoparticles under visible light irradiation. The pure MB solution without any photocatalyst as blank test showed no photolysis under visible light irradiation within 150 min, indicating that MB molecules were highly stable under visible light irradiation. The photocatalytic efficiency of ZnO nanoparticles was 25.71%. The Ho-doped ZnO nanoparticles showed the photocatalytic efficiency higher than the pure ZnO nanoparticles. The results show that Ho^{3+} ion played the role in enhancing the photocatalytic activity of ZnO. The photocatalytic efficacies in degrading of MB were increased to 89.24%, 96.66% and 83.95% for 1%, 3% and 5% Ho-doped ZnO nanoparticles, respectively. Among them, 3% Ho-doped ZnO nanoparticles played the highest role in degrading of MB under visible light irritation due to the highest surface area of active sites for photocatalytic reaction in accordance with the BET analysis. The high specific surface area can lead to increase the surface active sites and enhance the photocatalytic activity. The reaction kinetics of MB degradation over ZnO and Ho-doped ZnO nanoparticles under visible light irradiation were also investigated by the Langmuir–Hinshelwood model and the results are shown in Fig. 8b [1,7,8,19,23]. They show

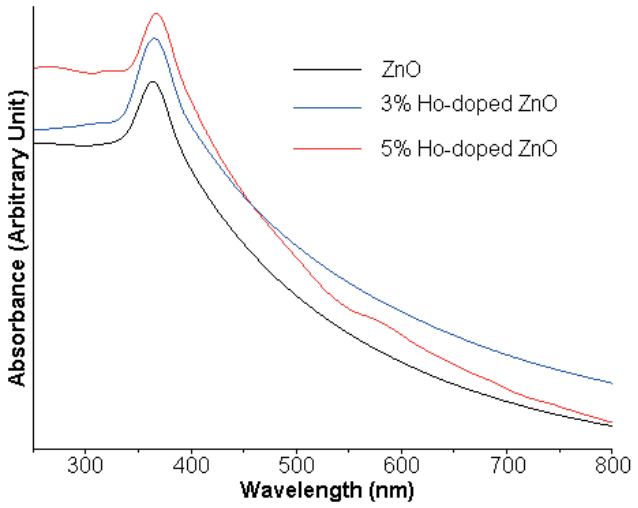

Fig. 6. UV-visible absorption of ZnO, 3% Ho-doped ZnO and 5% Ho-doped ZnO samples.

the linear plot with $R^2 \rightarrow 1$, indicating that the model kinetics for MB degradation over photocatalysts correspond to the first order reaction kinetics [1,7,8,19,23]. The reaction kinetics for MB degradation over photocatalysts were 2.01×10^{-3}, 0.0148, 0.0224 and 0.0115 min^{-1} for 0%, 1%, 3% and 5% Ho-doped ZnO nanoparticles, respectively. The 3% Ho-doped ZnO nanoparticles show the highest activity in degrading of MB. The efficiency of 3% Ho-doped ZnO nanoparticles is 11 times that of pure ZnO nanoparticles due to the higher number of oxygen vacancies and surface defects, electron–hole regeneration efficiency and charge trapping effect [9,11,14,15,17,19,22,23,26]. The photocatalytic efficiency was deceased when the content of Ho dopant is higher than 3% because the oxygen vacancies and defects became the recombination centers to inhibit the charge separation and reduce the photocatalytic reaction [9,11,14,46,47]. According to the photoluminescence (PL) analysis, the recombination rate of electron-hole of ZnO was decreased by the doped Ho. Fig. 9 shows the PL spectra of ZnO and Ho-doped ZnO nanoparticles. In

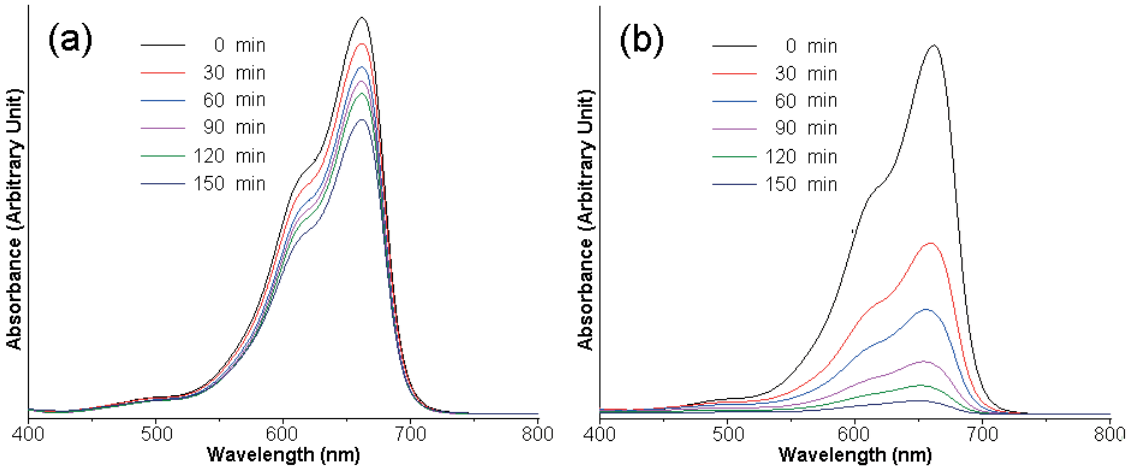

Fig. 7. (a) UV-visible absorption of MB solutions photocatalyzed by ZnO and (b) 3% Ho-doped ZnO nanoparticles under visible light irradiation.

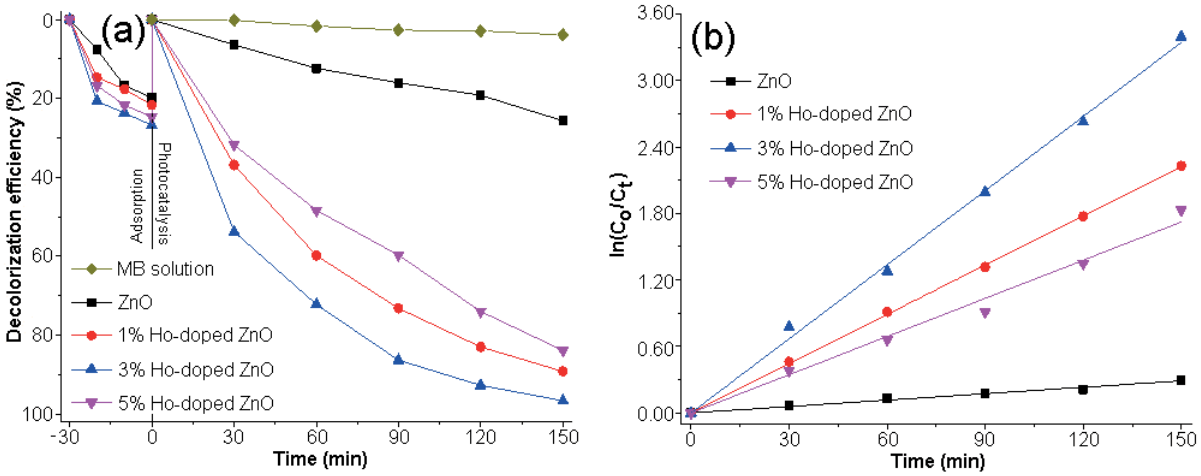

Fig. 8. (a) Decolorization efficiency and (b) reaction kinetics of 0%–5% Ho-doped ZnO nanoparticles in degrading of MB solutions illuminated by visible light comparing with decolorization of MB solution without a photocatalyst.

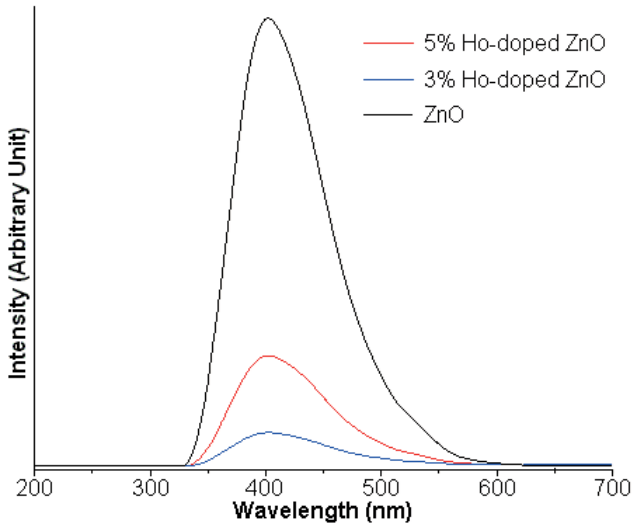

Fig. 9. PL spectra of 0%–5% Ho-doped ZnO nanoparticles.

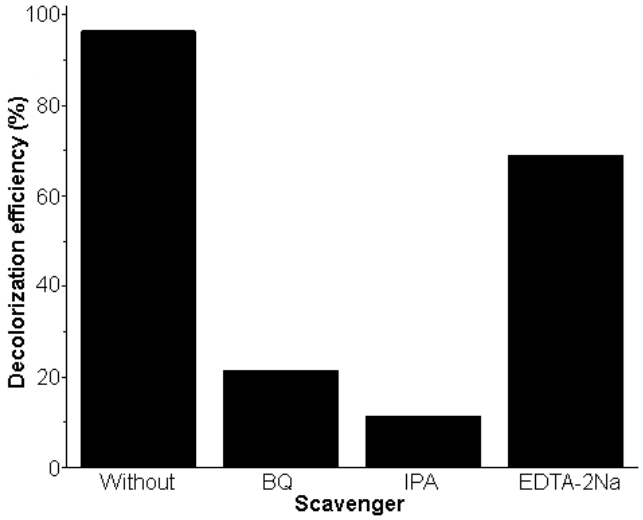

Fig. 10. Effect of different scavengers on the degradation of MB solutions photocatalyzed by 3% Ho-doped ZnO nanoparticles under visible light irradiation.

this research, the 3% Ho-doped ZnO nanoparticles have the lowest PL intensity. The rate of electron–hole recombination of 3% Ho-doped ZnO nanoparticles was less than those of ZnO and 5% Ho-doped ZnO nanoparticles [48,49]. According to the TOC analysis, the mineralization of the MB solution over 3% Ho-doped ZnO nanoparticles under visible light irradiation within 150 min was 60.32% or 3.28 times that of the MB solution over ZnO nanoparticles.

The active species generated during photocatalytic reaction were h^+, $^\bullet OH$ and $^\bullet O_2^-$ and were used to degrade MB over 3% Ho-doped ZnO nanoparticles under visible light irradiation. They were investigated and discussed. The scavenging reagents such as ethylenediaminetetraacetic acid disodium salt (EDTA-2Na), isopropanol (IPA) and benzoquinone (BQ) were also added to the MB solution to trap h^+, $^\bullet OH$ and $^\bullet O_2^-$ during the photocatalytic reaction [10,40,41,50,51]. Fig. 10 shows the photodegradation of MB over 3% Ho-doped ZnO nanoparticles in the presence and absence of the scavengers. When IPA and BQ were added, the photocatalytic efficacies in degrading of MB were considerably decreased to 11.35% and 21.32%, respectively. The results indicate that $^\bullet OH$, and $^\bullet O_2^-$ are the main and the first runner-up active species used to degrade MB over 3% Ho-doped ZnO nanoparticles under visible light irradiation. During photocatalysis, the surface of Ho-doped ZnO nanoparticles absorbed the photon. Subsequently, electrons were excited from valence band to conduction band and holes were induced in valence band [3,8,10,17,18,22]. The photo-excited electrons diffused to the surface and reacted with the adsorbed oxygen to form $^\bullet O_2^-$ radicals. Concurrently, the photo-induced holes reacted with the adsorbed H_2O/OH^- to form $^\bullet OH$ radicals [3,8,10,17,18,22]. In this case, the Ho^{3+} ions acted as electron sinks to prevent the recombination process, therefore, the photocatalytic reaction of ZnO under visible light irradiation was enhanced [17,18,22,23]. Then, the $^\bullet OH$, and $^\bullet O_2^-$ active species played the role in transforming MB molecules into CO_2 and H_2O [3,8,10,18,22,23].

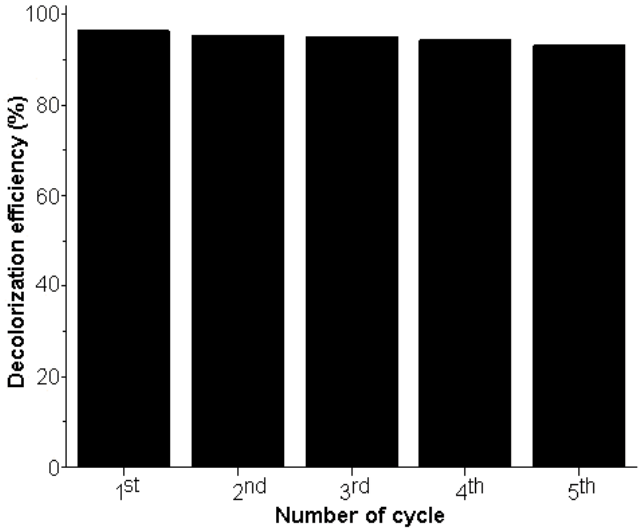

Fig. 11. Stability and recyclability of the reused 3% Ho-doped ZnO nanoparticles illuminated by visible light within five cycles.

In order to investigate reusability of the 3% Ho-doped ZnO nanoparticles, these nanoparticles were reused for photocatalysis for five cycles as the results shown in Fig. 11. In the experiment, the 3% Ho-doped ZnO nanoparticles were collected, washed and dried for being reused for the next cyclic reaction. At the end of cycle five, the photocatalytic efficiency of reused 3% Ho-doped ZnO nanoparticles slightly decreased from 96.66% to 93.21%, indicating that the 3% Ho-doped ZnO nanoparticles were very stable for the dye degradation.

4. Conclusions

In summary, Ho-doped ZnO nanoparticles with different weight contents of Ho dopant were synthesized by

tartaric acid combustion method. The analytical results of samples showed that ZnO and Ho-doped ZnO nanoparticles were pure phase of hexagonal wurtzite ZnO structure. The 3% Ho-doped ZnO nanoparticles have the highest efficiency in photodegrading of MB of 96.66% under visible light irradiation because the Ho^{3+} dopant acted as an electronic sink, and played the role in inhibiting the recombination of charge carrier pairs and enhancing the photocatalytic performance of ZnO under visible light irradiation. The 3% Ho-doped ZnO nanoparticles are very stable for the dye degradation.

Declaration of competing interest

The authors declare that they have no known competing financial interests or personal relationships that could have appeared to influence the work reported in this paper.

Acknowledgements

The research was supported by Prince of Songkla University under contract number SCI6402026S and the Center of Excellence in Materials Science and Technology, Chiang Mai University, Thailand.

References

[1] H. Parangusan, D. Ponnamma, M.A.A. Al-Maadeed, A. Marimuthu, Nanoflower-like yttrium-doped ZnO photocatalyst for the degradation of methylene blue dye, Photochem. Photobio., 94 (2018) 237–246.
[2] D.M. Shahi, S.A. Hassanzadeh-Tabrizi, A. Saffar-Teluri, Microemulsion synthesis, optical and photocatalytic properties of vanadium-doped nano ZnO, Int. J. Appl. Ceram. Technol., 15 (2018) 479–488.
[3] H.A. Rafaie, N.A.A.M. Nazam, N.In.T. Ramli, R. Mohamed, M.F. Kasim, Synthesis, characterization and photocatalytic activities of Al-doped ZnO for degradation of methyl orange dye under UV light irradiation, J. Aust. Ceram. Soc., 57 (2021) 479–488.
[4] S. Asadzadeh-Khaneghah, A. Habibi-Yangjeh, g-C_3N_4/carbon dot-based nanocomposites serve as efficacious photocatalysts for environmental purification and energy generation: a review, J. Cleaner Prod., 276 (2020) 124319.
[5] A. Akhundi, A. Habibi-Yangjeh, M. Abitorabi, S.R. Pouran, Review on photocatalytic conversion of carbon dioxide to value-added compounds and renewable fuels by graphitic carbon nitride-based photocatalysts, Catal. Rev. Sci. Eng., 61 (2019) 595–628.
[6] A. Habibi-Yangjeh, S. Asadzadeh-Khaneghah, S. Feizpoor, A. Rouhi, Review on heterogeneous photocatalytic disinfection of waterborne, airborne, and foodborne viruses: can we win against pathogenic viruses?, J. Colloid Interface Sci., 580 (2020) 503–514.
[7] A. Phuruangrat, B. Kuntalue, S. Thongtem, T. Thongtem, Hydrothermal synthesis of hexagonal ZnO nanoplates used for photodegradation of methylene blue, Optik, 226 (2021) 165949.
[8] A. Phuruangrat, S. Thongtem, T. Thongtem, Ultrasonic-assisted synthesis and photocatalytic performance of ZnO nanoplates and microflowers, Mater. Des., 107 (2016) 250–256.
[9] S. Shahbazkhany, M. Salehi, M. Mousavi-Kamazani, Facile synthesis, characterization, and decolorization activity of Mn^{2+} and Al^{3+} co-doped hexagonal-like ZnO nanostructures as photocatalysts, Appl. Organometal. Chem., 34 (2020) e5346.
[10] X. Chen, Z. Wu, D. Liu, Z. Gao, Preparation of ZnO photocatalyst for the efficient and rapid photocatalytic degradation of azo dyes, Nanoscale Res. Lett., 12 (2017) 143.
[11] N.T. Nguyen, V.A. Nguyen, Synthesis, characterization, and photocatalytic activity of ZnO nanomaterials prepared by a green, nonchemical route, J. Nanomater., 2020 (2020) 1768371.
[12] K.A. Isai, V.S. Shrivastava, Photocatalytic degradation of methylene blue using ZnO and 2%Fe–ZnO semiconductor nanomaterials synthesized by sol–gel method: a comparative study, SN Appl. Sci., 1 (2019) 1247.
[13] J. Kaur, S. Bansal, S. Singhal, Photocatalytic degradation of methyl orange using ZnO nanopowders synthesized via thermal decomposition of oxalate precursor method, Phys. B, 416 (2013) 33–38.
[14] S.H. Ferreira, M. Morais, D. Nunes, M.J. Oliveira, A. Rovisco, A. Pimentel, H. Águas, E. Fortunato, R. Martins, High UV and sunlight photocatalytic performance of porous ZnO nanostructures synthesized by a facile and fast microwave hydrothermal method, Materials, 14 (2021) 2385.
[15] Z. Zhou, J. Wang, C.G. Jhun, ZnO nanospheres fabricated by mechanochemical method with photocatalytic properties, Catalysts, 11 (2021) 572.
[16] L. Saikia, D. Bhuyan, M. Saikia, B. Malakar, D.K. Dutta, P. Sengupta, Photocatalytic performance of ZnO nanomaterials for self sensitizeddegradation of malachite green dye under solar light, Appl. Catal. A, 490 (2015) 42–49.
[17] A.M. Saad, M.R. Abukhadra, S.A.K. Ahmed, A.M. Elzanaty, A.H. Mady, M.A. Betiha, J.J. Shim, A.M. Rabie, Photocatalytic degradation of malachite green dye using chitosan supported ZnO and Ce–ZnO nano-flowers under visible light, J. Environ. Manage., 258 (2020) 110043.
[18] G. Flores-Carrasco, M. Rodríguez-Peña, A. Urbieta, P. Fernández, M.E. Rabanal, ZnO nanoparticles with controllable Ce content for efficient photocatalytic degradation of MB synthesized by the polyol method, Catalysts, 11 (2021) 71.
[19] S. Sanguanprang, A. Phuruangrat, T. Thongtem, S. Thongtem, Characterization and photocatalysis of visible-light-driven Dy-doped ZnO nanoparticles synthesized by tartaric acid-assisted combustion method, Inorg. Chem. Commun., 117 (2020) 107944.
[20] A. Khataee, R.D.C. Soltani, Y. Hanifehpour, M. Safarpour, H.G. Ranjbar, S.W. Joo, Synthesis and characterization of dysprosium-doped ZnO nanoparticles for photocatalysis of a textile dye under visible light irradiation, Ind. Eng. Chem., Res. 53 (2014) 1924–1932.
[21] A.R. Khataee, A. Karimi, R.D.C. Soltani, M. Safarpour, Y. Hanifehpour, S.W. Joo, Europium-doped ZnO as a visible light responsive nanocatalyst: sonochemical synthesis, characterization and response surface modeling of photocatalytic process, Appl. Catal. A, 488 (2014) 160–170.
[22] Y. Zong, Z. Li, X. Wang, J. Ma, Y. Men, Synthesis and high photocatalytic activity of Eu-doped ZnO nanoparticles, Ceram. Int., 40 (2014) 10375–10382.
[23] S. Selvaraj, M.K.M.M. Navaneethana, S. Ponnusamy, C. Muthamizhchelvan, Synthesis and photocatalytic activity of Gd doped ZnO nanoparticles for enhanced degradation of methylene blue under visible light, Mater. Sci. Semicond. Process., 103 (2019) 104622.
[24] O. Yayapao, T. Thongtem, A. Phuruangrat, S. Thongtem, Synthesis and characterization of highly efficient Gd doped ZnO photocatalyst irradiated with ultraviolet and visible radiations, Mater. Sci. Semicond. Process., 39 (2015) 786–792.
[25] Sukriti, P. Chand, V. Singh, Enhanced visible-light photocatalytic activity of samarium-doped zinc oxide nanostructures, J. Rare Earths, 38 (2020) 29–38.
[26] S.A. Ayon, M.M. Billah, S.S. Nishat, A. Kabir, Enhanced photocatalytic activity of Ho^{3+} doped ZnO NPs synthesized by modified sol–gel method: an experimental and theoretical investigation, J. Alloys Compd., 856 (2020) 158217.
[27] H. Cai, G. Liu, W. Lü, X. Li, L. Yu, D. Li, Effect of Ho-doping on photocatalytic activity of nanosized TiO_2 catalyst, J. Rare Earths, 26 (2008) 71–75.
[28] X. Liu, P. Fang, Y. Liu, Z. Liu, D. Lu, Y. Gao, F. Chen, D. Wang, Y. Dai, Effect of holmium doping on the structure and photocatalytic behavior of TiO_2-based nanosheets, J. Mater. Sci., 49 (2014) 8063–8073.

[29] G. Gaidamavičienė, A. Žalga, Synthesis, a structural and thermoanalytical study of $Ca_{1-x}Sr_xMoO_4$ ceramic, Mater. Chem. Phys., 241 (2020) 122339.
[30] P. Visuttipitukul, P. Sooksaen, N. Yongvanich, Sol–gel synthesis of $SrTiO_3$ nanoparticles using acetic acid as a chelating agent, Ferroelectrics, 457 (2013) 82–88.
[31] Powder Diffract. File, JCPDS-ICDD, 12 Campus Boulevard, Newtown Square, PA 19073–3273, U.S.A., 2001.
[32] W.J. Evans, Tutorial on the role of cyclopentadienyl ligands in the discovery of molecular complexes of the rare-earth and actinide metals in new oxidation states, Organometallics, 35 (2016) 3088−3100.
[33] S. Yin, V. Sharma, A. McDannald, F.A. Reboredo, M. Jain, Magnetic and magnetocaloric properties of iron substituted holmium chromite and dysprosium chromite, RSC Adv., 6 (2016) 9475–9483.
[34] N. Rama, J.B. Philipp, M. Opel, A. Erb, V. Sankaranarayanan, R. Gross, M.S. Ramachandra Rao, Effect of rare earth ion substitution on the magnetic and transport properties of $Pr_{0.7}RE_{0.04}Sr_{0.26}MnO_3$ (RE = Er^{3+}, Tb^{3+} and Ho^{3+}), Eur. Phys. J. B, 38 (2004) 553–557.
[35] M. Rabiei, A Palevicius, A. Monshi, S. Nasiri, A. Vilkauskas, G. Janusas, Comparing methods for calculating nano crystal size of natural hydroxyapatite using X-ray diffraction, Nanomaterials, 10 (2020) 1627.
[36] U. Holzwarth, N. Gibson, The Scherrer equation versus the 'Debye–Scherrer equation', Nat. Nanotechnol., 6 (2011) 534.
[37] X. Xue, W. Ruan, L. Yang, W. Ji, Y. Xie, L. Chen, W. Song, B. Zhao, J.R. Lombardi, Surface-enhanced Raman scattering of molecules adsorbed on Co-doped ZnO nanoparticles, J. Raman Spectrosc., 43 (2012) 61–64.
[38] X. Guo, H. Guo, Y. Wang, Y. Li, L. Liu, H. Li, H. Lian, Y. Cheng, Synthesis of novel Ho_2O_3–Fe_2O_3 porous nanotubes and their ultra-high acetone-sensing properties, J. Porous Mater., 25 (2018) 1757–1763.
[39] L. Pavasaryte, S. Balu, T.C.K. Yang, Synthesis of sol–gel derived holmium aluminium garnet on exfoliated g-C_3N_4: a novel visible-light-driven Z-scheme photocatalyst for the degradation of sunset yellow FCF, J. Mater. Sci., 30 (2019) 20132–20143.
[40] P. Intaphong, A. Phuruangrat, H. Yeebu, K. Akhbari, T. Sakhon, S. Thongtem, T. Thongtem, Sonochemical synthesis of Pd nanoparticle/ZnO flower photocatalyst used for methylene blue and methyl orange degradation under UV radiation, Russ. J. Inorg. Chem., 66 (2021) 2123–2133.
[41] A. Phuruangrat, A. Nunpradit, T. Sakhon, P. Dumrongrojthanath, N. Ekthammathat, S. Thongtem, T. Thongtem, Microwave-assisted synthesis of heterostructure Pd/ZnO flowers used for photocatalytic reaction of dyes illuminated by UV radiation, J. Aust. Ceram. Soc., 57 (2021) 1521–1530.
[42] W. Marimón-Bolívar, E.E. González, Study of agglomeration and magnetic sedimentation of Glutathione@Fe_3O_4 nanoparticles in water medium, Rev. DYNA, 85 (2018) 19–26.
[43] A. Phuruangrat, W. Kongpet, O. Yayapao, B. Kuntalue, S. Thongtem, T. Thongtem, Ultrasonic-assisted synthesis, characterization, and optical properties of Sb doped ZnO and their photocatalytic activities, J. Nanomater., 2014 (2014) 725817.
[44] S.N. Ogugua, O.M. Ntwaeaborwa, H.C. Swart, Luminescence, structure and insight on the inversion degree from normal to inverse spinel in a $ZnAl_{(2-x)}Fe_x^{3+}O_4$ system, Bol. Soc. Esp. Ceram., 60 (2021) 147–162.
[45] J. Singh, S. Kaur, G. Kaur, S. Basu, M. Rawat, Biogenic ZnO nanoparticles: a study of blueshift of optical band gap and photocatalytic degradation of reactive yellow 186 dye under direct sunlight, Green Process. Synth., 8 (2019) 272–280.
[46] P. Hemalatha, S.N. Karthick, K.V. Hemalatha, M. Yi, H.J. Kim, M. Alagar, La-doped ZnO nanoflower as photocatalyst for methylene blue dye degradation under UV irradiation, J. Mater. Sci., 27 (2016) 2367–2378.
[47] I. Ahmad, M.S. Akhtar, E. Ahmed, M. Ahmad, Facile synthesis of Pr-doped ZnO photocatalyst using sol–gel method and its visible light photocatalytic activity, J. Mater. Sci., 31 (2020) 1084–1093.
[48] G. Hosseinzadeh, H. Rasoulnezhad, N. Ghasemian, R. Hosseinzadeh, Ultrasonic-assisted spray pyrolysis technique for synthesis of transparent S-doped TiO_2 thin film, J. Aust. Ceram. Soc., 55 (2019) 387–394.
[49] G.K. Sukhadeve, S.Y. Janbandhu, S. Upadhyay, R.S. Gedam, Investigation of photocatalytic activity of TiO_2 nanoparticles synthesized by sol–gel technique, J. Aust. Ceram. Soc., 58 (2022) 39–48.
[50] A.R. Kuldeep, R.S. Dhabbe, K.M. Garadkar, Development of g-C_3N_4-TiO_2 visible active hybrid photocatalyst for the photodegradation of methyl orange, Res. Chem. Intermed., 47 (2021) 5155–5174.
[51] Y. Si, Y. Chen, M. Xu, X. Zhang, F. Zuo, Q. Yan, Synthesis and characterization of Z-scheme Ag_2WO_4/Bi_2MoO_6 heterojunction photocatalyst: enhanced visible-light photodegradation of organic pollutant, J. Mater. Sci., 31 (2020) 1191–1199.